



## Article

# Visual/Photoelectrochemical Off-On Sensor Based on Cu/Mn Double-Doped CeO<sub>2</sub> and Branched Sheet Embedded Cu<sub>2</sub>O/CuO Nanocubes

Huihui Shi <sup>1</sup>, Yanfei Che <sup>1</sup>, Yumeng Rong <sup>1</sup>, Jiajun Wang <sup>1</sup>, Yanhu Wang <sup>2</sup>, Jinghua Yu <sup>1</sup>  and Yan Zhang <sup>1,3,\*</sup> <sup>1</sup> School of Chemistry and Chemical Engineering, University of Jinan, Jinan 250022, China<sup>2</sup> Shandong Analysis and Test Center, Qilu University of Technology (Shandong Academy of Sciences), Jinan 250014, China<sup>3</sup> Key Laboratory of Optic-Electric Sensing and Analytical Chemistry for Life Science, MOE, Qingdao University of Science and Technology, Qingdao 266042, China

\* Correspondence: chm\_zhangyan@hotmail.com

**Abstract:** An integrated dual-signal bioassay was devised to fulfil thrombin (TB) ultrasensitive detection by integrating visualization with the photoelectrochemical technique based on G-quadruplex/hemin. During the process, branched sheet embedded copper-based oxides prepared with illumination and alkaline condition play a vital role in obtaining the desirable photocurrent. The switchover of photoelectrochemical signal was realized by the adjustable distance between electron acceptor G-quadruplex/hemin and interface materials due to dissociation of the Cu/Mn double-doped cerium dioxide (CuMn@CeO<sub>2</sub>)/DNA caused by the addition of TB. Then, CuMn@CeO<sub>2</sub> transferred onto visual zones triggered catalytic reactions under the existence of 3,3',5,5'-tetramethylbenzidine and hydrogen peroxide, making a variation in color recognized by the naked eye and providing visual prediction. Under optimized conditions, this bioassay protocol demonstrated wide linear ranges (0.0001–50 nM), high selectivity, stability, and reproducibility. More importantly, the proposed visual/photoelectrochemical transduction mechanism platform exhibits a lower background signal and more reliable detection results, which also offers an effective way for detecting other proteins and nucleic acids.

**Keywords:** photoelectrochemical; colorimetric; thrombin; paper-based device; Cu<sub>2</sub>O/CuO; CuMn@CeO<sub>2</sub>



**Citation:** Shi, H.; Che, Y.; Rong, Y.; Wang, J.; Wang, Y.; Yu, J.; Zhang, Y. Visual/Photoelectrochemical Off-On Sensor Based on Cu/Mn Double-Doped CeO<sub>2</sub> and Branched Sheet Embedded Cu<sub>2</sub>O/CuO Nanocubes.

*Biosensors* **2023**, *13*, 227. <https://doi.org/10.3390/bios13020227>

Received: 23 November 2022

Revised: 27 January 2023

Accepted: 2 February 2023

Published: 4 February 2023



**Copyright:** © 2023 by the authors. Licensee MDPI, Basel, Switzerland. This article is an open access article distributed under the terms and conditions of the Creative Commons Attribution (CC BY) license (<https://creativecommons.org/licenses/by/4.0/>).

## 1. Introduction

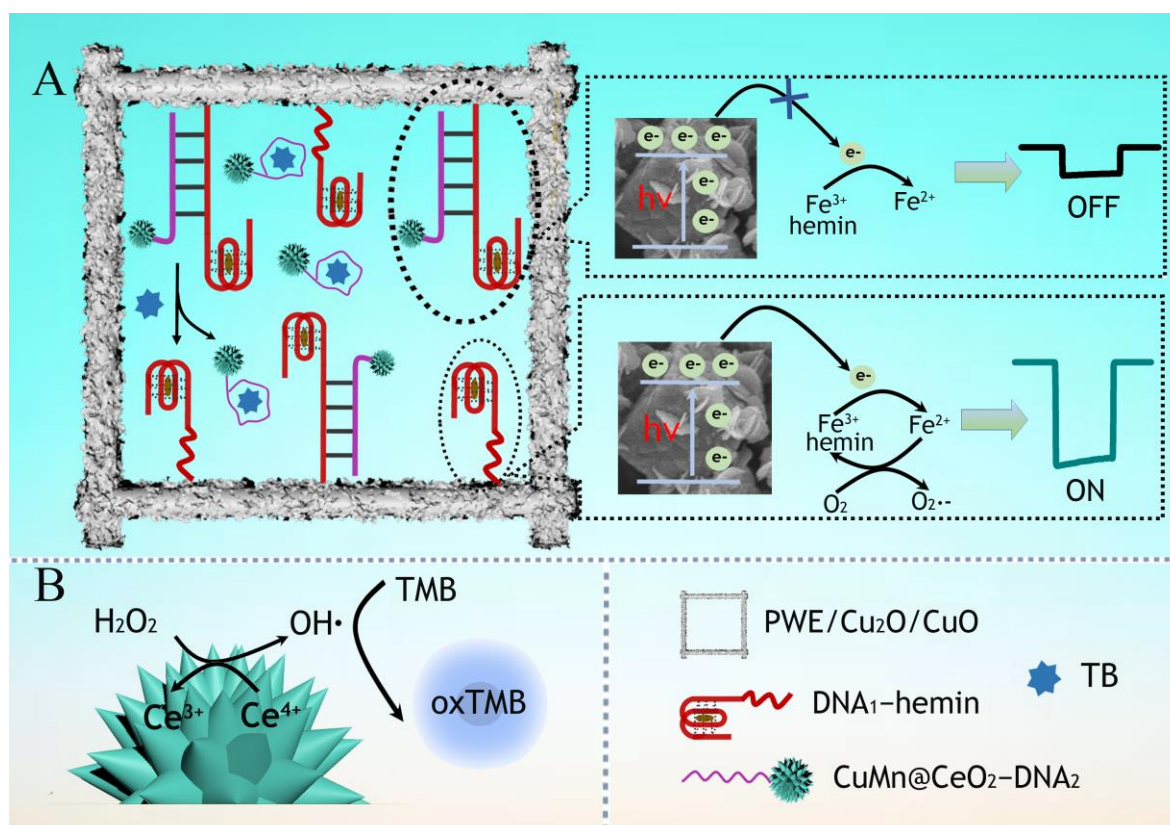
Thrombin (TB), as a member of the serine protease group, has been identified to be expressed in various cardiovascular diseases including cerebral ischemia and infarction. Considering the importance of TB assays, an efficient sensing strategy for fast and sensitive TB detection is highly desired [1,2]. Up to now, numerous analytical methods were reported, including chemiluminescence [3], electrochemiluminescence [4,5], fluorescence [6], electrochemistry [7,8], and photoelectrochemistry (PEC) [9,10]. Among these protocols, PEC, as an emerged analytical method with high sensitivity and a low background signal, has received substantial attention [11,12]. However, most of them relied on a signal output model, which still need to be improved to decrease the influence of systematic error. To achieve a more accurate and reliable analysis, an alternative method is to combine a naked-eye colorimetric strategy with the PEC transduction mechanism.

As an essential portion in colorimetric reaction and the PEC process, nanomaterials with catalytic and photoactive activity have a great impact on the obtained signal strength [13–16]. Cerium oxide (CeO<sub>2</sub>), simultaneously existing Ce<sup>3+</sup> and Ce<sup>4+</sup> oxidation states on the lattice surface, could catalyze 3,3',5,5'-tetramethylbenzidine (TMB) to convert colorless to blue with assistance of H<sub>2</sub>O<sub>2</sub> due to oxygen vacancy [17,18]. However, the capacity is relatively low to be used for low-concentration analytes detection. It is a good

method to dope CeO<sub>2</sub> with metal to expand their application as colorimetric reaction probes [19,20]. As a consequence, double-doped CeO<sub>2</sub> (CuMn@CeO<sub>2</sub>) was prepared with superior catalytic performance for more accurate detection. Furthermore, to obtain a desirable PEC signal, a cuprous oxide–cupric oxide (Cu<sub>2</sub>O/CuO) composite was introduced as a photoactive material owing to its abundance, affordable price, environmental acceptability, and low band-gap energy [21,22]. The fabrication process was carried out under normal temperature and pressure, with low-cost and high-quality products. The introduction of an external stimulus can promote the reduction process significantly, and the obtained Cu<sub>2</sub>O in such a strong redox photochemical surrounding possessed the intrinsic superiority to endure photocorrosion in a kinetically more favorable way [23]. Furthermore, the well-designed overall architecture of the branched sheet embedded nanocubic Cu<sub>2</sub>O/CuO complex not only provides more active sites and a larger surface area, but also helps Cu<sub>2</sub>O to overcome its high carrier recombination caused by short electron diffusion length (20–100 nm) [24,25].

Apart from desirable initial PEC performance, an efficient electron transfer-regulated strategy is also of vital importance in broadening the application range of the PEC system [9,26]. G-quadruplex/hemin, which forms between single-stranded guanine-rich aptamer and hemin, has been utilized to act as an electron acceptor and mediate the catalytic reduction of dissolved oxygen [9,27]. Thus, this special structure could be employed as an effective way to realize off-on transformation in the PEC detecting process. In addition, to operate the whole process, an easy-to-operate platform was necessary. Cellulose paper, owning virtues of unique structure, low cost, large specific surface area, and portability, has aroused widespread interest [28–30]. Concretely, it is easy to be folded to satisfy diverse demand when applied as micro-reactors. Combined with the abovementioned factors, an integrated paper-based platform was fabricated to functionalize the working electrode and implement a multi-module microfluidic device.

Hence, a dual-signal output paper-based sensing strategy integrating the PEC technique with visualization in two spatially separated working areas, gold nanoparticles (AuNPs)-modified PEC working electrodes (PWE) and visual areas, was proposed for TB detection (Scheme 1). Concretely, TMB and H<sub>2</sub>O<sub>2</sub> were applied on the visual areas for chromogenic reactions, while branched sheet-like nanocubic Cu<sub>2</sub>O/CuO and hemin-DNA<sub>1</sub> were applied on the PWE surface with excellent PEC performance due to G-quadruplex/hemin. With addition of Cu/Mn-doped cerium dioxide/DNA<sub>2</sub> (CuMn@CeO<sub>2</sub>-DNA<sub>2</sub>), the specific double-stranded structure based on hybridization of DNA<sub>1</sub> and DNA<sub>2</sub> and steric hindrance of CuMn@CeO<sub>2</sub> could dramatically decrease the photocurrent, thus the “signal-off” trend for PEC signal can be triggered. After that, with the application of TB, DNA<sub>2</sub> could hybridize with TB, causing free CuMn@CeO<sub>2</sub>-DNA<sub>2</sub>. Then, the released CuMn@CeO<sub>2</sub> could catalyze H<sub>2</sub>O<sub>2</sub> on visual areas, forming the hydroxyl radical that can make TMB effectively develop colors, which offers visual prediction for thrombin concentration. Meanwhile, due to a DNA<sub>2</sub>-TB binding event, dissociation of CuMn@CeO<sub>2</sub> facilitated the electrons transfer and G-quadruplex/hemin could accept electrons from the illuminated Cu<sub>2</sub>O/CuO, resulting in the increase of PEC intensity and switchover from off to on mode of the PEC signal. Such a distance-based PEC sensing system between electron acceptor and interface materials endows detection methods with lower background signal. Accordingly, the paper-based analytical device with a dual-signal output sensing mechanism was successfully fabricated, which could be introduced as quantitative platform for screening of other proteins and nucleic acids.



**Scheme 1.** Schematic illustration of (A) off–on switchover of PEC areas and (B) visual detection of TB.

## 2. Experimental Section

### 2.1. Design of Paper-Based Device

The prepared whole device was made with four units: detection tab, photoreaction auxiliary tab, fluid transfer tab, and electrode tab, as depicted in Figure 1A,B. Two working zones (8 mm in diameter) for the establishment of the sensing platform were patterned on the detection tab (I for PEC system, II for chromogenic reaction). In order to form a densely distributed nanosized oxide layer, more growth solution that exceeded the capacity of a single working area was required. Thus, the photoreaction auxiliary tab, where the white area was designed to be hollow while the green area is hydrophobic, was added to the device to hold more solutions in the light reaction process after folding (Figure 1C). When the device was folded as shown in Figure 1D, the branch channel (3.0 mm × 5.0 mm) on the fluid transfer tab is favorable to connect two working zones which are ready for fluid transfer. The carbon working electrode (WE) was printed on the back of the detection zone, while the carbon counter electrode (CE) and Ag/AgCl reference electrode (RE) are on the hydrophilic zone (8 mm in diameter) of the electrode tab. Finally, a three-dimensional device for visual and PEC detection was successfully constructed after the electrode tab folded under the detection tab, as displayed in Figure 1E.

### 2.2. Preparation of CuMn@CeO<sub>2</sub>-DNA<sub>2</sub>

Firstly, 0.1 g CuMn@CeO<sub>2</sub> (the synthesis process can be found in the Supporting Information) was redispersed in 10 mL ethanol and stirred for 30 min. Then, 0.1 mL 3-aminopropyltriethoxysilane was injected into the above solution and refluxed at 70 °C for 90 min. After the obtained solution was centrifugated and washed with ethanol and deionized water, 100 µL glutaraldehyde (1%, *w/w*) was added to activate the amino groups on the CuMn@CeO<sub>2</sub> surface. To obtain CuMn@CeO<sub>2</sub>-modified DNA<sub>2</sub>, 15 µL of DNA<sub>2</sub> was first added in the dispersed 2 mL CuMn@CeO<sub>2</sub> solution with stirring for 12 h at 4 °C.

Next, the above solution was diluted with 25 mM Tris-HCl and 0.3 M NaCl, followed by centrifugation at 12,000 rpm for 10 min to remove unconjugated DNA. The resultant CuMn@CeO<sub>2</sub>-DNA<sub>2</sub> was stored at 4 °C when not in use.

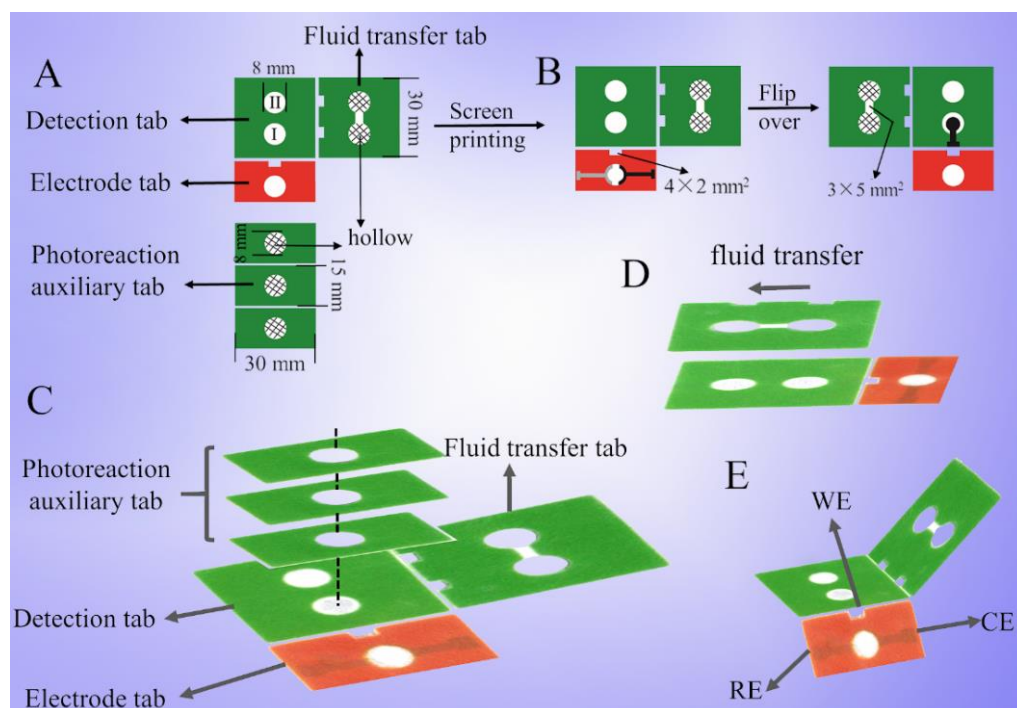


**Figure 1.** Schematic layout of (A) prepared device and (B) the fabricated device with screen–printed electrodes. Assembly illustration of prepared device during (C) photoreaction, (D) fluid transfer, and (E) sensing platform.

### 2.3. Fabrication of Dual-Signal Sensing Platform

PWE were prepared as shown in the Supporting Information. In order to achieve a desirable PEC signal, nanocubic Cu<sub>2</sub>O was first coated on PWE by the light-induced photochemical synthesis approach [23]. Briefly, 1 mL as-prepared copper tungstate (CuWO<sub>4</sub>) solution (0.15 M, the preparation process can be found in the Supporting Information) was coated onto PWE by a spin coater, then 50 µL solution containing 0.3 M NaOH and 0.1 M glucose was dropped onto the surface of PWE with a photoreaction auxiliary unit. Next, the assembled photochemical reaction device was irradiated by a 300W Xe lamp for 60 min and then rinsed with distilled water. After that, the electrode dealt with 50 µL 0.2 M NaOH for 30 min. Subsequently, 50 µL chitosan aqueous solution (0.08 wt%) in 1% acetic acid was applied onto the working electrode and reacted for 60 min. After drying, 5 wt% glutaraldehyde was added to activate the electrode, and the final electrode was denoted as PWE/Cu<sub>2</sub>O/CuO. Finally, 20 µL acetic acid (pH 4.5), 20 mM TMB, and 20 µL of 0.5 M H<sub>2</sub>O<sub>2</sub> were dropped onto the II visual area.

### 2.4. Analysis Process of TB

The dual-signal mechanism detection was performed by the following procedure. Firstly, 50 µL of 1 µM DNA<sub>1</sub> and 1 µM hemin was dropped onto the PWE and kept for 80 min, followed by adding 50 µL of 1 µM CuMn@CeO<sub>2</sub>-DNA<sub>2</sub>. After the PEC electrode was incubated with different concentrations of TB for 50 min, the device was folded as depicted in Figure 1D and the above mixed solution's fluid flow from PWE to the II visual zone could be generated along the hydrophilic channel on the fluid transfer tab. The electrode was carefully cleaned with 0.01 M phosphate buffer saline (PBS, pH 7.4) after each step. Finally, color variance could be signaled and the PEC signal was recorded by a three-electrode system (−0.1 V).



### 3. Results and Discussion

#### 3.1. Structure Characterization

The morphology evolution of nanomaterials was investigated by scanning electron microscope (SEM) as illustrated in Figure 2. Clearly, it could be found that interconnected fibers of the bare sample zone displayed porous architecture with high surface area (Figure 2A), which provided a special micro-environment for AuNPs' growth. Pyknotic AuNPs were modified onto the cellulose by an in situ growth technique and they were distributed onto the fibers' surface uniformly (Figure 2B). Moreover, the conductivity of the paper-based electrode was measured by a four-probe tester (Agilent U1251B multimeter), with the results shown in Figure S1. Significantly, PWE displayed lower resistance ( $0.385 \Omega$ ) than that of new clean FTO ( $2.017 \Omega$ ) and ITO ( $1.337 \Omega$ ). Then, deposition of  $\text{Cu}_2\text{O}/\text{CuO}$  on the PWE was conducted by an in situ synthesis approach with two steps. To better survey the preparation process of the  $\text{Cu}_2\text{O}$ , samples were gathered at diverse stages of photochemical reaction time. At first, layered substances (Figure S2A) with a particle structure were clearly observed adsorbing on the surface of the PWE. After 15 min irradiation, a small amount of crystals similar to microcubes were sparsely distributed on the fibers (Figure S2B). To additionally probe the existing elements, energy-dispersive X-ray spectroscopy (EDS) and element mapping analysis were performed. Clearly, it could be seen that peaks of tungsten are observed in the EDS spectra (Figure S3) for working electrodes and Figure S2B<sub>1</sub>–B<sub>4</sub> reveals that Cu, W, O, and C elements were uniformly distributed on the fibers. Hence, layered substances were presumed to be  $\text{CuWO}_4$ . In addition, with the increase of illumination time, the distribution of cubes became more and more intensive until it reached optimum at the photoreaction time of 60 min (Figures S2C,D and 2D). Only Cu, O, and C peaks were collected for PWE/ $\text{Cu}_2\text{O}$  (Figure 2C) and they were evenly distributed on the fibers (Figure 2E). The fact that no spectrum pertaining to the tungsten element was found in EDS patterns of electrodes with 60 min photoreaction time demonstrated that  $\text{CuWO}_4$  was gradually converted to oxides of microcubes with the increase of photoreaction time. The more microscopic morphology of cubes was observed by zoom-in SEM with  $\sim 400$  nm diameter (inset in Figure 2D). Moreover, there was a sparse distribution of cubes on the PWE (Figure S2E) without the photoreaction auxiliary unit for photochemical processes, verifying that the existence of the photoreaction auxiliary unit was necessary. The separate working electrode only has a growth fluid capacity of  $50 \mu\text{L}$ , whereas the electrode with the photoreaction auxiliary unit could hold up to  $1.0 \text{ mL}$ . Moreover, the SEM image of the working electrode without illumination showed unsatisfactory performance (Figure S2F), illustrating the necessity of illumination. In the subsequent reaction process under alkaline condition,  $\text{Cu}_2\text{O}$  in cubes was gradually partly transformed into intersecting sheet  $\text{CuO}$  (Figure 2F).

The phase structure and the crystallization details of the sample were further researched with X-ray diffraction (XRD) and Raman spectroscopy. A peak at  $22.89^\circ$  gathered from the original working zone of the paper-based device was assigned to (002) planes of cellulose [31], as depicted in Figure 3A. For PWE, four additional peaks at  $38.18$ ,  $44.39$ ,  $64.58$ , and  $77.55^\circ$  were well-matched with characteristic peaks of Au NPs (JCPDS 04-0784). Except for naked papers and Au NPs peaks, other distinguishable peaks in curve c could be well-indexed to the pristine cubic phase of  $\text{Cu}_2\text{O}$  shown in Figure S4A. The PWE/ $\text{Cu}_2\text{O}/\text{CuO}$  electrode exhibited apparent diffractions of cubic  $\text{Cu}_2\text{O}$  and additional diffraction peaks at  $35.49^\circ$  of  $\text{CuO}$ , illustrating successful preparation of  $\text{Cu}_2\text{O}/\text{CuO}$ . Furthermore, Raman spectra of above electrodes were shown in Figure 3B. Similar to that of cellulose paper, no obvious characteristic peaks were recorded in the Raman pattern of PWE. After the first photoreaction, three peaks were collected for the  $\text{Cu}_2\text{O}$ -functionalized PWE. Peaks at  $217$  and  $636 \text{ cm}^{-1}$  resulted from the second-order Raman-allowed mode and the red-allowed mode of  $\text{Cu}_2\text{O}$ , meanwhile another presented at  $413 \text{ cm}^{-1}$  corresponding to the four-phonon mode. Both  $\text{Cu}_2\text{O}$  and  $\text{CuO}$  peaks were recorded simultaneously for PWE/ $\text{Cu}_2\text{O}/\text{CuO}$ . Apart from the peak of  $\text{Cu}_2\text{O}$  at  $217 \text{ cm}^{-1}$ , the other three peaks at  $280$ ,  $326$ , and  $617 \text{ cm}^{-1}$

were assigned to Ag, Bg, and Bg mode of CuO. All these peaks exhibited sharpness, indicating preferable crystallization of the synthesized materials.

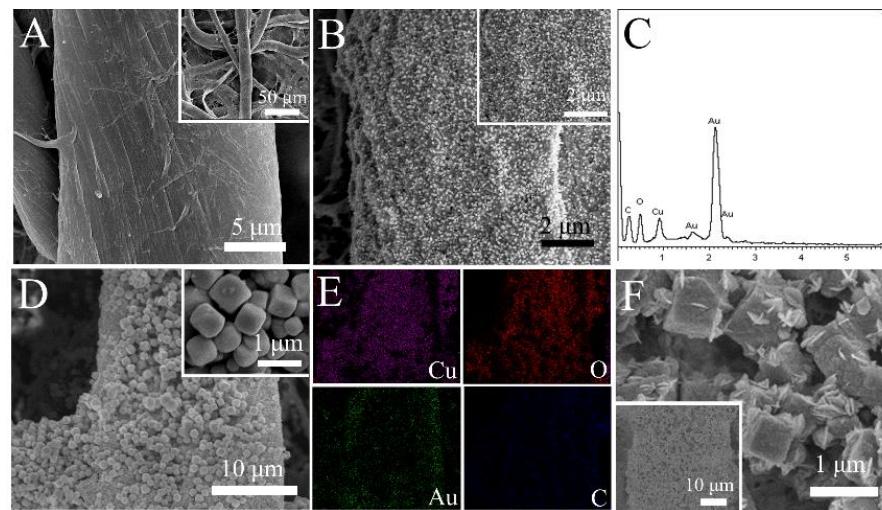


**Figure 2.** SEM images of (A) sample zone, (B) PWE, (D) PWE/Cu<sub>2</sub>O, and (F) PWE/Cu<sub>2</sub>O/CuO at different magnifications. (C) EDS and (E) elemental mappings of PWE/Cu<sub>2</sub>O.

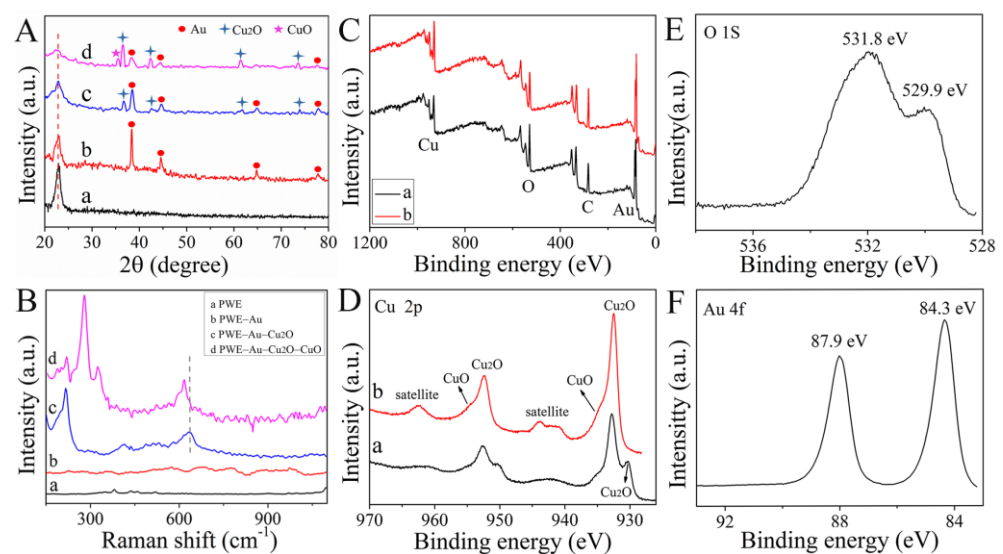


**Figure 3.** (A) XRD patterns and (B) Raman spectra (a) cellulose paper, (b) PWE, (c) PWE/Cu<sub>2</sub>O, and (d) PWE/Cu<sub>2</sub>O/CuO. (C) XPS survey scan of (a) PWE/Cu<sub>2</sub>O and (b) PWE/Cu<sub>2</sub>O/CuO. (D) High-resolution XPS spectra of Cu 2p of (a) PWE/Cu<sub>2</sub>O and (b) PWE/Cu<sub>2</sub>O/CuO. High-resolution XPS spectra of (E) O 1s and (F) Au 4f of PWE/Cu<sub>2</sub>O/CuO.

X-ray photoelectron spectroscopy experiments were further operated to gain chemical composition information of the PWE/Cu<sub>2</sub>O and PWE/Cu<sub>2</sub>O/CuO. As shown in Figure 3C, the presence of Cu, O, and Au elements could be attributed to the product of the photochemical reaction and conductive Au NPs. To explore the chemical state of the Cu element, the Cu 2p core-level spectra of PWE/Cu<sub>2</sub>O and PWE/Cu<sub>2</sub>O/CuO were compared as displayed in Figure 3D. For Cu<sub>2</sub>O-modified PWE, the characteristic peaks at the binding energies of 932.8 and 952.6 eV were associated with the Cu 2p<sub>3/2</sub> and Cu 2p<sub>1/2</sub> of Cu<sub>2</sub>O, respectively [32]. As a contrast, PWE/Cu<sub>2</sub>O/CuO showed two additional obvious peaks at 934.8 and 954.6 eV, which corresponded to Cu 2p<sub>3/2</sub> and Cu 2p<sub>1/2</sub> of CuO. Additionally, three weak satellite peaks at 940.8, 943.8, and 962.3 eV originated from multiple excitations in copper oxides and were attributed to the open 3d<sup>9</sup> shell of Cu<sup>2+</sup> in CuO [33]. As shown in

Figure 3E, the peak at 529.9 eV was related to the lattice oxygen from both  $\text{Cu}_2\text{O}$  and  $\text{CuO}$  phases and the other peak at 531.8 eV marked the surface hydroxyl group, which was consistent with the reported literature [34]. Moreover, Au 4f 7/2 and Au 4f 5/2 peaks presented at 84.3 and 87.9 eV were observed (Figure 3F), which were similar to the counterpart for the standard Au (0) [35]. Moreover, the solution's color change in the whole process was also favorable evidence for the successful preparation of  $\text{Cu}_2\text{O}/\text{CuO}$  (Figure S4B). All of these results matched each other, demonstrating the successful fabrication of PWE/ $\text{Cu}_2\text{O}/\text{CuO}$ .

### 3.2. Ce-Based Materials Characterization

The SEM technique was characterized to explore the morphology of the beacon in colorimetric reactions. Obviously, uniform-size nanospheres with a rough surface were found and the average size of  $\text{CuMn@CeO}_2$  was around 60 nm (Figure 4A). To probe the elements, EDS and mapping were conducted, with the results displayed in Figure 4B,C, respectively. It could be observed that Ce, Cu, Mn, and O elements were collected and they were evenly distributed in the nanospheres. Furthermore, the main peak of  $\text{CeO}_2$  in Raman spectra at about  $463\text{ cm}^{-1}$  was attributed to the  $\text{F}_{2g}$  Raman mode (Figure 4D). Compared with that of pure  $\text{CeO}_2$ , the peak shifts to lower frequency at around  $459\text{ cm}^{-1}$ , indicating occurrence of defects in the  $\text{CeO}_2$  lattice structure after doping with Cu and Mn metals [36]. Meanwhile, additional peaks at 368 and  $544\text{ cm}^{-1}$  were collected, which correspond to oxygen vacancies for  $\text{CuMn@CeO}_2$ , confirming that extra oxygen vacancies existed in  $\text{CuMn@CeO}_2$  with excellent catalytic performance.

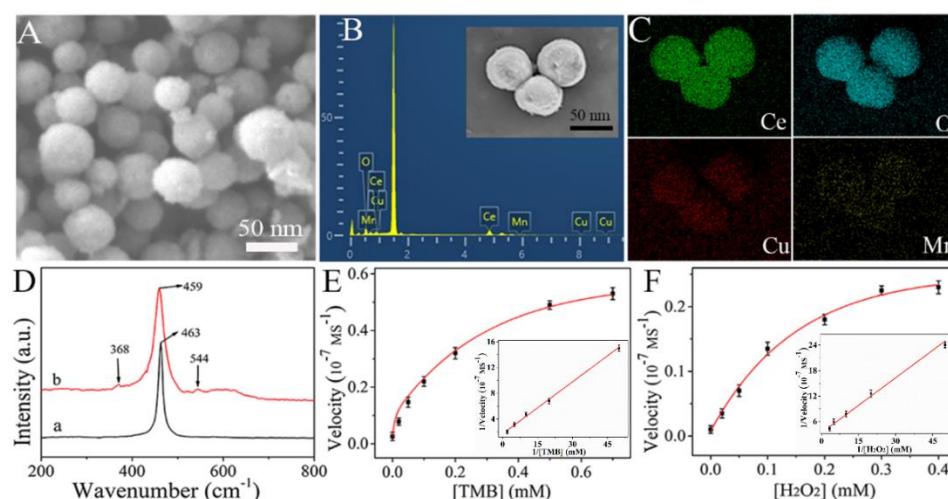


**Figure 4.** (A) SEM image, (B) EDS, and (C) mapping of  $\text{CuMn@CeO}_2$ . (D) Raman spectra of (a)  $\text{CeO}_2$  and (b)  $\text{CuMn@CeO}_2$ . Michaelis–Menten curves at (E) fixed concentration of  $\text{H}_2\text{O}_2$  (2 mM) and various concentrations of TMB (0–0.7 mM) and (F) fixed concentration of TMB (0.6 mM) and various concentrations of  $\text{H}_2\text{O}_2$  (0–0.4 mM) (inset: corresponding Lineweaver–Burk plots).

Additionally, steady-state kinetic constants measurement experiments were carried out to verify catalytic performances of  $\text{CuMn@CeO}_2$  (Figure 4E,F). During the process, TMB and  $\text{H}_2\text{O}_2$  concentration were variables. Obtained data were fitted by the Michaelis–Menten kinetic equation,  $v = (v_{\text{max}} \times [\text{S}]) / (\text{K}_m + [\text{S}])$ , where a smaller  $\text{K}_m$  value means a higher affinity of enzyme to substrate. Compared with that of horseradish peroxidase ( $\text{K}_m(\text{H}_2\text{O}_2) = 3.7\text{ mM}$ ,  $\text{K}_m(\text{TMB}) = 0.434\text{ mM}$ ), the values for  $\text{CuMn@CeO}_2$  towards  $\text{H}_2\text{O}_2$  and TMB were 0.15 mM and 0.12 mM, indicating that  $\text{CuMn@CeO}_2$  had a stronger affinity for  $\text{H}_2\text{O}_2$  and TMB than enzyme and provided accessible active sites for analytes.

### 3.3. EIS and PEC Behavior

Electrochemical impedance spectroscopy (EIS) was an effective technique to verify the manufacturing procedure of the sensing platform [37]. As magnified in Figure 5A,

PWE showed a small electron-transfer resistance ( $R_{et}$ ) due to great conductivity of AuNPs (curve a). With the nanomaterial modification progress, the  $R_{et}$  increased dramatically for PWE/Cu<sub>2</sub>O and PWE/Cu<sub>2</sub>O/CuO (curves b and c) due to low conductivity of Cu<sub>2</sub>O and CuO. As expected, the  $R_{et}$  showed an upward trend when hemin-DNA<sub>1</sub> and CuMn@CeO<sub>2</sub>-DNA<sub>2</sub> were attached onto the PWE surface in turn (curves d and e). It could be explained as the steric hindrance of hemin-DNA<sub>1</sub> and CuMn@CeO<sub>2</sub>-DNA<sub>2</sub> that prevented the charge-transfer rate of redox. Furthermore, the transient photocurrent responses of modified PWE were monitored. As revealed in Figure 5B, PWE/Cu<sub>2</sub>O/CuO (curve b) displayed an obvious enhancement of PEC recovery compared with PWE/Cu<sub>2</sub>O (curve a) due to the heterojunction formation of Cu<sub>2</sub>O/CuO. Significantly, PEC performance of a paper-based electrode with greater immobilization capacity for photoelectric materials caused by special three-dimensional interlaced fibers was superior to FTO/ITO-based electrodes (Figure S5). As the electrode incubated with hemin-DNA<sub>1</sub>, the value of photocurrent increased dramatically due to the presence of G-quadruplex/hemin (curve c). With the addition of CuMn@CeO<sub>2</sub>-DNA<sub>2</sub>, a reduced photocurrent was acquired (curve d) caused by enhanced steric hindrance and reduced electron transfer efficiency, indicating that the biosensor was successfully prepared as expected.

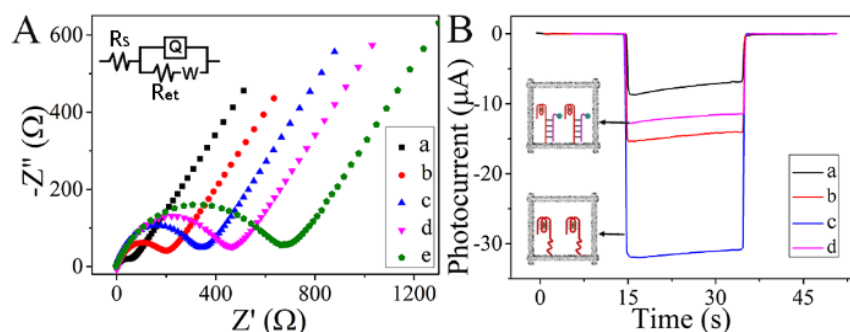


**Figure 5.** (A) EIS spectra of (a) PWE, (b) PWE/Cu<sub>2</sub>O, (c) PWE/Cu<sub>2</sub>O/CuO, (d) PWE/Cu<sub>2</sub>O/CuO/hemin–DNA<sub>1</sub>, and (e) PWE/Cu<sub>2</sub>O/CuO/hemin–DNA<sub>1</sub>/CuMn@CeO<sub>2</sub>–DNA<sub>2</sub> in 5 mM [Fe(CN)<sub>6</sub>]<sup>3−/4−</sup> solution containing 0.1 M KCl. (B) Photocurrent responses of (a) PWE/Cu<sub>2</sub>O, (b) PWE/Cu<sub>2</sub>O/CuO, (c) PWE/Cu<sub>2</sub>O/CuO/hemin–DNA<sub>1</sub>, and (d) PWE/Cu<sub>2</sub>O/CuO/hemin–DNA<sub>1</sub>/CuMn@CeO<sub>2</sub>–DNA<sub>2</sub> in 0.01 M PBS solution.

### 3.4. Analytical Performance

The well-designed signal output paper-based device was employed to realize the quantitative detection by analyzing the PEC signals and color intensity with the variety of TB concentrations. Excellent catalytic performances toward H<sub>2</sub>O<sub>2</sub> of CuMn@CeO<sub>2</sub> can offer visual prediction for analytes. Under optimal conditions (Figure S6), color intensity and photocurrent witnessed an upward trend along with the elevated concentration of TB, and a dynamic range was obtained from 0.0001 to 50 nM (Figure 6A,B). Meanwhile, the excellent linear relationship between logarithmic value of TB concentrations (Figure 6C) and photocurrent response could be fitted and the linear regression was  $-\Delta I_{PEC} (\mu A) = 2.30 \lg c + 10.99$  ( $R = 0.994$ ), and the detection limit was calculated as 0.035 pM ( $S/N = 3$ ). Compared with single-signal readout strategies (Table 1), the paper-based visual/PEC biosensor exhibited apparent merits in wide response range and dual-signal sensing mode, providing a more accurate and effective method for TB detection.

### 3.5. Specificity, Stability, and Reproducibility

To further assess the feasibility of the present protocol, three significant criterions for biosensors, the selectivity, stability, and reproducibility, were explored. The specificity of the dual-signal bioassay was investigated by incubation with 0.1 nM TB, human immunoglobulin G (HIgG), carcinoembryonic antigen (CEA), bovine serum albumin (BSA), and their mixture. The highest photocurrent response was obtained for samples containing



TB (Figure 7A), demonstrating gratifying specificity. The stability of the as-prepared sensing device was measured by applying 0.1 nM TB as samples and monitoring the photocurrent responses intermittently (every 2 days). As expected, experimental results revealed acceptable stability (Figure 7B). Furthermore, the reproducibility was investigated by testing five independent electrodes, and the relative standard deviation of photocurrent response was 4.3%, demonstrating acceptable precision and repeatability.

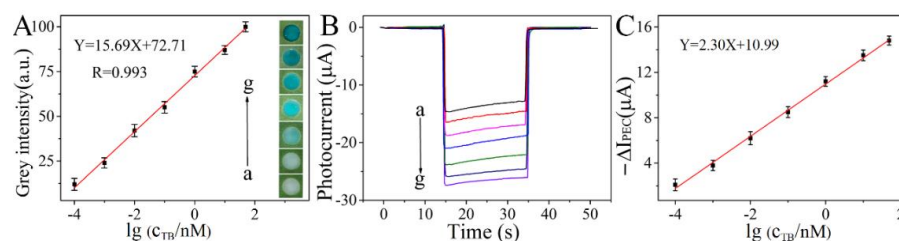


**Figure 6.** (A) Calibration curve between color intensity and logarithm of TB concentration (inset: color intensity). (B) Photocurrent of sensing device at different TB concentrations (0.0001, 0.001, 0.01, 0.1, 1, 10, 50 nM) and (C) corresponding calibration curve between  $-\Delta I_{PEC}$  and logarithm of TB concentration.

**Table 1.** Comparison of the biosensor with other analytical strategies.

Method	Materials	Linear Range (nM)	Detection Limit (pM)	References
Electrochemiluminescence	Graphene oxide and carbon nanotubes	0.001–5	0.23	[38]
Electrochemical	Au NPs	0.005–50	1.1	[39]
Electrochemical	Au electrode and methylene blue	0.005–1	1.7	[40]
Fluorescence	Zinc selenide quantum dots	0.1–20	25	[41]
PEC	Au-ZnO Nanoflowers	0.001–30	0.37	[7]
Visual/PEC	Cu <sub>2</sub> O/CuO and CuMn@CeO <sub>2</sub>	0.0001–50	0.035	This work

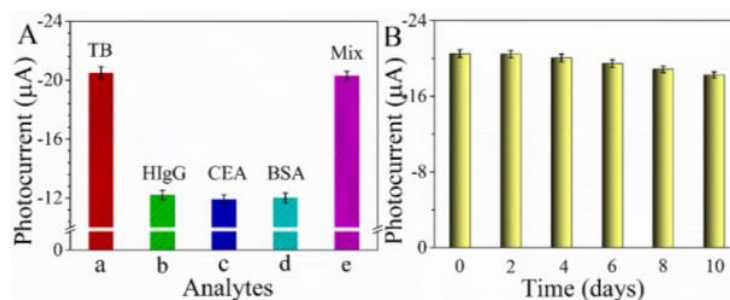


**Figure 7.** (A) Photocurrent of the bioassay in the presence of 0.1 nM sample. (B) Photocurrent responses of constructed PEC sensing platform with 0.1 nM TB.

#### 4. Conclusions

Herein, Cu/Mn-doped CeO<sub>2</sub> and branched sheet embedded Cu-based nanocubes were prepared for fabrication of an effective visual/PEC paper-based sensing platform to obtain sensitive analysis of TB. The rapid chromogenic reactions were achieved by the release of CuMn@CeO<sub>2</sub> with the addition of TB, which provides a simple visual prediction. Meanwhile, the presence of TB led to dissociation of CuMn@CeO<sub>2</sub> and the electrons-acceptable distance of G-quadruplex/hemin, which then contributed to the switchover of the original PEC signal caused by branched sheet embedded nanocubic Cu<sub>2</sub>O/CuO. Undoubtedly, such dual-signal output strategy with good performance was capable of making detection results more sensitive and accurate. Additionally, it was anticipated that the approach shows potentiality in designing numerous biosensors with excellent performance for analytes detection.

**Supplementary Materials:** The following supporting information can be downloaded at: <https://www.mdpi.com/article/10.3390/bios13020227/s1>, Figure S1: Physical photos of (A) FTO, (B) ITO, and (C) PWE sheet resistance; Figure S2: SEM images of PWE with photoreaction progresses at (A) 0 min, (C) 30 min, (D) 45 min. (B–B4) Elemental mappings of PWE with photoreaction progresses at 15 min. SEM images of (E) PWE/Cu<sub>2</sub>O without photoreaction auxiliary unit and (F) the electrode without illumination; Figure S3: EDS spectra of PWE with photoreaction progresses at 15 min; Figure S4: (A) XRD pattern of Cu<sub>2</sub>O and CuO. (B) Photographs of photoreaction progresses at (a) 0 min, (b) 15 min, (c) 30 min, (d) 45 min and (e) 60 min; and (f) the obtained Cu<sub>2</sub>O/CuO photograph; Figure S5: Photocurrent response of (a) FTO/Cu<sub>2</sub>O/CuO, (b) ITO/Cu<sub>2</sub>O/CuO, and (c) PWE/Cu<sub>2</sub>O/CuO; Figure S6: Effect of TB incubation time. References [42,43] are cited in the Supplementary Materials.

**Author Contributions:** H.S.: Conceptualization, methodology, investigation, and writing—original draft. Y.C.: Investigation and data curation. Y.R.: Methodology and investigation. J.W.: Data curation. Y.W.: Investigation, formal analysis. Y.Z.: Investigation, writing—reviewing and editing, resources. J.Y.: Funding acquisition, project administration. All authors have read and agreed to the published version of the manuscript.

**Funding:** This work was financially supported by the National Natural Science Foundation of China (21874055, 21904047), Taishan Scholars Program (tsqn202103082), the Excellent Youth Innovation Team in Universities of Shandong (2021KJ021), Science and Technology Program of University of Jinan (XKY2203), and the Open Fund of Key Laboratory of Optic-electric Sensing and Analytical Chemistry for Life Science, MOE, Qingdao University of Science and Technology (M2023-5).

**Institutional Review Board Statement:** Not applicable.

**Informed Consent Statement:** Not applicable.

**Data Availability Statement:** Not applicable.

**Conflicts of Interest:** The authors declare no conflict of interest.

## References

1. Li, M.; Zheng, Y.; Liang, W.; Yuan, Y.; Chai, Y.; Yuan, R. An ultrasensitive “on-off-on” photoelectrochemical aptasensor based on signal amplification of a fullerene/CdTe quantum dots sensitized structure and efficient quenching by manganese porphyrin. *Chem. Commun.* **2016**, *52*, 8138–8141. [[CrossRef](#)] [[PubMed](#)]
2. Shao, C.; Chi, J.; Chen, Z.; Cai, L.; Zhao, Y. Superwetable colloidal crystal micropatterns on butterfly wing surface for ultrasensitive detection. *J. Colloid Interf. Sci.* **2019**, *546*, 122–129. [[CrossRef](#)]
3. Sun, Y.; Zhu, X.; Liu, H.; Dai, Y.; Han, R.; Gao, D.; Luo, C.; Wang, X.; Wei, Q. Novel chemiluminescence sensor for thrombin detection based on dual-aptamer biorecognition and mesoporous silica encapsulated with iron porphyrin. *ACS Appl. Mater. Interfaces* **2020**, *12*, 5569–5577. [[CrossRef](#)]
4. Fang, Y.; Wang, H.M.; Gu, Y.X.; Yu, L.; Wang, A.J.; Yuan, P.X.; Feng, J.J. Highly enhanced electrochemiluminescence luminophore generated by zeolitic imidazole framework-8-linked porphyrin and its application for thrombin detection. *Anal. Chem.* **2020**, *92*, 3206–3212. [[CrossRef](#)] [[PubMed](#)]
5. Shao, K.; Wang, B.; Ye, S.; Zuo, Y.; Wu, L.; Li, Q.; Lu, Z.; Tan, X.; Han, H. Signal-amplified near-infrared ratiometric electrochemiluminescence aptasensor based on multiple quenching and enhancement effect of graphene/gold nanorods/G-quadruplex. *Anal. Chem.* **2016**, *88*, 8179–8187. [[CrossRef](#)] [[PubMed](#)]
6. Zhao, X.; Li, S.; Xu, L.; Ma, W.; Wu, X.; Kuang, H.; Wang, L.; Xu, C. Up-conversion fluorescence “off-on” switch based on heterogeneous core-satellite assembly for thrombin detection. *Biosens. Bioelectron.* **2015**, *70*, 372–375. [[CrossRef](#)]
7. Yang, Z.H.; Zhuo, Y.; Yuan, R.; Chai, Y.Q. Amplified thrombin aptasensor based on alkaline phosphatase and hemin/G-quadruplex-catalyzed oxidation of 1-naphthol. *ACS Appl. Mater. Interfaces* **2015**, *7*, 10308–10315. [[CrossRef](#)] [[PubMed](#)]
8. Heydari-Bafrooei, E.; Amini, M.; Ardakani, M.H. An electrochemical aptasensor based on TiO<sub>2</sub>/MWCNT and a novel synthesized Schiff base nanocomposite for the ultrasensitive detection of thrombin. *Biosens. Bioelectron.* **2016**, *85*, 828–836. [[CrossRef](#)]
9. Wang, G.L.; Shu, J.X.; Dong, Y.M.; Wu, X.M.; Zhao, W.W.; Xu, J.J.; Chen, H.Y. Using G-quadruplex/hemin to “switch-on” the cathodic photocurrent of p-type PbS quantum dots: Toward a versatile platform for photoelectrochemical aptasensing. *Anal. Chem.* **2015**, *87*, 2892–2900. [[CrossRef](#)] [[PubMed](#)]
10. Xu, F.; Zhu, Y.C.; Ma, Z.Y.; Zhao, W.W.; Xu, J.J.; Chen, H.Y. An ultrasensitive energy-transfer based photoelectrochemical protein biosensor. *Chem. Commun.* **2016**, *52*, 3034–3037. [[CrossRef](#)]
11. Wang, Z.J.; Li, Q.; Tan, L.L.; Liu, C.G.; Shang, L. Metal-organic frameworks-mediated assembly of gold nanoclusters for sensing applications. *J. Anal. Test.* **2022**, *6*, 163–177. [[CrossRef](#)] [[PubMed](#)]

12. Wang, F.; Fan, Q.; Wang, Y.; Wang, Y.; Ge, S.; Yan, M.; Yu, J. A paper-supported photoelectrochemical sensing platform based on surface plasmon resonance enhancement for real-time H<sub>2</sub>S determination. *J. Anal. Test.* **2019**, *3*, 89–98. [[CrossRef](#)]
13. Shi, X.M.; Fan, G.C.; Shen, Q.; Zhu, J.J. Photoelectrochemical DNA biosensor based on dual-signal amplification strategy integrating inorganic-organic nanocomposites sensitization with  $\lambda$ -exonuclease-assisted target recycling. *ACS Appl. Mater. Interfaces* **2016**, *8*, 35091–35098. [[CrossRef](#)] [[PubMed](#)]
14. Pravin, S.; Xiaoni, P.; Jue, W.; Yanxiao, M.; Louis, M.; Nathan, H.; Arunava, G.; Shanlin, P. Rapid screening of photoanode materials using scanning photoelectrochemical microscopy technique and formation of Z-scheme solar water splitting system by coupling p- and n-type heterojunction photoelectrodes. *ACS Appl. Energy Mater.* **2018**, *1*, 2283–2294.
15. Wang, B.; Mei, L.P.; Ma, Y.; Xu, Y.T.; Ren, S.W.; Cao, J.T.; Liu, Y.M.; Zhao, W.W. Photoelectrochemical-chemical-chemical redox cycling for advanced signal amplification: Proof-of-concept toward ultrasensitive photoelectrochemical bioanalysis. *Anal. Chem.* **2018**, *90*, 12347–12351. [[CrossRef](#)] [[PubMed](#)]
16. Jessica, C.B.; Charles, R.M. Scalable methods for device patterning as an outstanding challenge in translating paper-based microfluidics from the academic benchtop to the point-of-care. *J. Anal. Test.* **2019**, *3*, 50–60.
17. Tang, L.; Li, J. Plasmon-based colorimetric nanosensors for ultrasensitive molecular diagnostics. *ACS Sens.* **2017**, *2*, 857–875. [[CrossRef](#)]
18. Kong, Q.; Cui, K.; Zhang, L.; Wang, Y.; Sun, J.; Ge, S.; Zhang, Y.; Yu, J. “On–Off–On” Photoelectrochemical/Visual Lab-on-Paper Sensing via Signal Amplification of CdS Quantum Dots@Leaf-Shape ZnO and Quenching of Au-Modified Prism-Anchored Octahedral CeO<sub>2</sub> Nanoparticles. *Anal. Chem.* **2018**, *90*, 11297–11304. [[CrossRef](#)]
19. Cheng, X.; Huang, L.; Yang, X.; Elzatahry, A.; Alghamdi, A.; Deng, Y. Rational design of a stable peroxidase mimic for colorimetric detection of H<sub>2</sub>O<sub>2</sub> and glucose: A synergistic CeO<sub>2</sub>/Zeolite Y nanocomposite. *J. Colloid Interf. Sci.* **2019**, *535*, 425–435. [[CrossRef](#)]
20. Liu, W.; Liu, X.; Feng, L.; Guo, J.; Xie, A.; Wang, S.; Zhang, J.; Yang, Y. The synthesis of CeO<sub>2</sub> nanospheres with different hollowness and size induced by copper doping. *Nanoscale* **2014**, *6*, 10693–10700. [[CrossRef](#)]
21. Yang, Z.; Kang, T.; Ji, Y.; Li, J.; Zhu, Y.; Liu, H.; Jiang, X.; Zhong, Z.; Su, F. Architectural Cu<sub>2</sub>O@CuO mesocrystals as superior catalyst for trichlorosilane synthesis. *J. Colloid Interf. Sci.* **2021**, *589*, 198–207. [[CrossRef](#)] [[PubMed](#)]
22. Wu, S.; Fu, G.; Lv, W.; Wei, J.; Chen, W.; Yi, H.; Gu, M.; Bai, X.; Zhu, L.; Tan, C.; et al. A single-step hydrothermal route to 3D hierarchical Cu<sub>2</sub>O/CuO/rGO nanosheets as high-performance anode of lithium-ion batteries. *Small* **2018**, *14*, 1702667. [[CrossRef](#)] [[PubMed](#)]
23. Zhang, L.; Jing, D.; Guo, L.; Yao, X. In situ photochemical synthesis of Zn-doped Cu<sub>2</sub>O hollow microcubes for high efficient photocatalytic H<sub>2</sub> production. *ACS Sustain. Chem. Eng.* **2014**, *2*, 1446–1452. [[CrossRef](#)]
24. Jiang, D.; Xue, J.; Wu, L.; Zhou, W.; Zhang, Y.; Li, X. Photocatalytic performance enhancement of CuO/Cu<sub>2</sub>O heterostructures for photodegradation of organic dyes: Effects of CuO morphology. *Appl. Catal. B Environ.* **2017**, *211*, 199–204. [[CrossRef](#)]
25. Huang, Q.; Kang, F.; Liu, H.; Li, Q.; Xiao, X. Highly aligned Cu<sub>2</sub>O/CuO/TiO<sub>2</sub> core/shell nanowire arrays as photocathodes for water photoelectrolysis. *J. Mater. Chem. A* **2013**, *1*, 2418–2425. [[CrossRef](#)]
26. Zhao, W.W.; Xu, J.J.; Chen, H.Y. Photoelectrochemical bioanalysis: The state of the art. *Chem. Soc. Rev.* **2015**, *44*, 729–741. [[CrossRef](#)]
27. Shu, J.; Tang, D.P. Recent advances in photoelectrochemical sensing: From engineered photoactive materials to sensing devices and detection modes. *Anal. Chem.* **2020**, *92*, 363–377. [[CrossRef](#)]
28. Zhang, Y.; Zhang, L.; Cui, K.; Ge, S.; Cheng, X.; Yan, M.; Yu, J.; Liu, H. Flexible electronics based on micro/nanostructured paper. *Adv. Mater.* **2018**, *30*, 1801588. [[CrossRef](#)] [[PubMed](#)]
29. Hou, Y.; Lv, C.C.; Guo, Y.L.; Ma, X.H.; Liu, W.; Jin, Y.; Yao, S.Y. Recent advances and applications in paper-based devices for point-of-care testing. *J. Anal. Test.* **2022**, *6*, 247–273. [[CrossRef](#)]
30. Zhu, L.; Lv, X.; Yu, H.; Tan, X.; Rong, Y.; Feng, W.; Zhang, L.; Yu, J.; Zhang, Y. Paper-Based Bipolar Electrode Electrochemiluminescence Platform Combined with Pencil-Drawing Trace for the Detection of M.SssI Methyltransferase. *Anal. Chem.* **2022**, *94*, 8327–8334. [[CrossRef](#)]
31. Zhang, Y.; Li, Y.L.; Cui, S.H.; Wen, C.Y.; Li, P.; Yu, J.F.; Zeng, J.B. Distance-based detection of Ag<sup>+</sup> with gold nanoparticles coated microfluidic paper. *J. Anal. Test.* **2021**, *5*, 11–18. [[CrossRef](#)]
32. Shyamal, S.; Maity, A.; Satpati, A.K.; Bhattacharya, C. Amplification of PEC hydrogen production through synergistic modification of Cu<sub>2</sub>O using cadmium as buffer layer and dopant. *Appl. Catal. B Environ.* **2019**, *246*, 111–119. [[CrossRef](#)]
33. Cheng, S.; Delacruz, S.; Chen, C.; Tang, Z.; Shi, T.; Carraro, C.; Maboudian, R. Hierarchical Co<sub>3</sub>O<sub>4</sub>/CuO nanorod array supported on carbon cloth for highly sensitive non-enzymatic glucose biosensing. *Sens. Actuators B* **2019**, *298*, 126860. [[CrossRef](#)]
34. Li, H.; Su, Z.; Hu, S.; Yan, Y. Free-standing and flexible Cu/Cu<sub>2</sub>O/CuO heterojunction net: A novel material as cost-effective and easily recycled visible-light photocatalyst. *Appl. Catal. B Environ.* **2017**, *207*, 134–142. [[CrossRef](#)]
35. Yao, W.; Li, F.L.; Li, H.X.; Lang, J.P. Fabrication of hollow Cu<sub>2</sub>O@CuO-supported Au-Pd alloy nanoparticles with high catalytic activity through the galvanic replacement reaction. *J. Mater. Chem. A* **2015**, *3*, 4578–4585. [[CrossRef](#)]
36. Xue, S.; Li, Q.; Wang, L.; You, W.; Zhang, J.; Che, R. Copper- and cobalt-codoped CeO<sub>2</sub> nanospheres with abundant oxygen vacancies as highly efficient electrocatalysts for dual-mode electrochemical sensing of MicroRNA. *Anal. Chem.* **2019**, *91*, 2659–2666. [[CrossRef](#)]

37. Zhang, Y.; Xu, J.; Zhou, S.; Zhu, L.; Lv, X.; Zhang, J.; Zhang, L.; Zhu, P.; Yu, J. DNAzyme-triggered visual and ratiometric electrochemiluminescence dual-readout assay for Pb(II) based on an assembled paper device. *Anal. Chem.* **2020**, *92*, 3874–3881. [[CrossRef](#)] [[PubMed](#)]
38. Wu, D.; Xin, X.; Pang, X.; Pietraszkiewicz, M.; Hozyst, R.; Sun, X.; Wei, Q. Application of europium multiwalled carbon nanotubes as novel luminophores in an electrochemiluminescent aptasensor for thrombin using multiple amplification strategies. *ACS Appl. Mater. Interfaces* **2015**, *7*, 12663–12670. [[CrossRef](#)]
39. Qiu, F.; Gan, X.; Jiang, B.; Yuan, R.; Xiang, Y. Electrode immobilization-free and sensitive electrochemical sensing of thrombin via magnetic nanoparticle-decorated DNA polymers. *Sens. Actuators B Chem.* **2021**, *331*, 129395. [[CrossRef](#)]
40. Yang, J.; Dou, B.; Yuan, R.; Xiang, Y. Aptamer/protein proximity binding-triggered molecular machine for amplified electrochemical sensing of thrombin. *Anal. Chem.* **2017**, *89*, 5138–5143. [[CrossRef](#)]
41. Tian, Y.; Xin, C.; Liu, S.; Liu, Y.; Liu, S. Affinity binding-induced Hg<sup>2+</sup> release and quantum dot doping for general, label-free, and homogenous fluorescence protein assay. *ACS Sens.* **2018**, *3*, 1401–1408. [[CrossRef](#)] [[PubMed](#)]
42. Wang, H.; Jian, Y.; Kong, Q.; Liu, H.; Lan, F.; Liang, L.; Ge, S.; Yu, J. Ultrasensitive electrochemical paper-based biosensor for microRNA via strand displacement reaction and metal-organic frameworks. *Sens. Actuators B Chem.* **2018**, *257*, 561–569. [[CrossRef](#)]
43. Li, X.; Zhang, H.; Tang, Y.; Wu, P.; Xu, S.; Zhang, X. A both-end blocked peroxidase-mimicking DNAzyme for low-background chemiluminescent sensing of miRNA. *ACS Sens.* **2017**, *2*, 810–816. [[CrossRef](#)]

**Disclaimer/Publisher's Note:** The statements, opinions and data contained in all publications are solely those of the individual author(s) and contributor(s) and not of MDPI and/or the editor(s). MDPI and/or the editor(s) disclaim responsibility for any injury to people or property resulting from any ideas, methods, instructions or products referred to in the content.